

Pore-scale modelling of elastic properties in hydrate-bearing sediments using 4-D synchrotron radiation imaging

Rui Li^a, Yingfang Zhou^{a,b,d,*}, Wenbo Zhan^a, Jianhui Yang^c

^a University of Aberdeen, UK

^b The National IOR Centre of Norway, 4036, Norway

^c Geoscience Research Centre, Total E&P UK Limited, UK

^d School of Energy Resources, China University of Geosciences, Beijing 100083, China

ARTICLE INFO

Keywords:

Hydrate-bearing sediments

Elastic moduli

Elastic wave velocity

Pore-scale modelling

4-D hydrate morphology

ABSTRACT

Gas hydrate contains abundant methane gas, which is considered to be a promising energy resource to mitigate the influence of climate change in the future. Understanding the effect of fluids-solid-hydrate spatial distribution on elastic properties of hydrate-bearing sediments benefits the well-log interpretation. We constructed 4-D hydrate-bearing models covering a wide hydrate saturation range based on high-resolution digital images obtained by Synchrotron Radiation X-Rays Computed Tomography (SRXCT). We analysed the elastic moduli and elastic wave velocities of these models by the static Finite Element Method (FEM). The results demonstrated that the dominant hydrate morphology transits from pore-filling to load-bearing when hydrate saturation increases. At low hydrate saturations, the hydrate formed around some gas bubbles blocks local pore space. Therefore a great enhancement in compressional wave velocity was observed at low hydrate saturations. While the shear wave velocity was less affected due to the presence of thin water films. Based on the simulated results, an empirical model was developed to compute the compressional and shear wave velocities considering the free gas phase. The comparison with some experimental measurements validated the applicability of the model.

1. Introduction

Gas hydrate, widely distributed in continental margin settings and onshore permafrost under low temperatures and high pressure conditions, has been considered as a potential energy resource that could contribute to the energy transition towards a low carbon society (Boswell and Collett, 2011). The global reserves (gas in place) of natural gas stored in gas hydrate reaches $3 \sim 24.8 \times 10^{15} \text{ m}^3$, which is approximately twice as the carbon stored in conventional fossil fuel deposits, including coal, oil and natural gas reserves (Kvenvolden, 1993). Gas hydrate may also play a significant role in areas such as climate change and geologic hazards (Waite et al., 2009). In exploring hydrate deposits, elastic moduli (bulk and shear modulus) and elastic wave velocities (compressional and shear wave velocity) prove to be critical factors in confirming the presence of hydrate in the sediments (Waite et al., 2009; Goldberg et al., 2010). Previous studies have shown that the presence of hydrate can stiffen the host sediments and thus the elastic properties vary with hydrate saturation (Stoll, 1974; Priest et al., 2005; Faisal et al., 2017; Jakobsen et al., 2000; Dvorkin and Nur, 1996;

Dvorkin et al., 1999; Sahoo et al., 2018a; Liu et al., 2018). Seismic tools were widely used for detecting the presence of a bottom simulating reflector (BSR), which proved to be the major way to identify potential gas hydrate reserves (Moridis et al., 2011; Spence et al., 2010). Therefore, a proper understanding of the relation between elastic properties and hydrate saturation is essential.

Studies of hydrate-bearing sediments and its geophysical properties have been implemented via field cores retrieved by pressure coring techniques (Holland et al., 2019; Jin et al., 2016; Santamarina et al., 2012; Dai and Santamarina, 2014; Oshima et al., 2019; Boswell et al., 2019) and synthetic samples in the laboratory (Tohidi et al., 2001; Sahoo et al., 2018b; Stoll and Bryan, 1979; Bian et al., 2022; Priest et al., 2009; Lee et al., 2007). Different imaging techniques have been applied to probe the hydrate distribution within the host sediments, such as X-Ray computed tomography (Kerker et al., 2009, 2014; Lei et al., 2018; Chaouachi et al., 2015), cryogenic scanning electron microscopy (CSEM) (Winters et al., 2014), and magnetic resonance imaging (MRI) (Kleinberg et al., 2003; Xue et al., 2012; Bagherzadeh et al., 2011). A few conceptual models have been proposed to describe hydrate pore habits

* Corresponding author. University of Aberdeen, UK.
E-mail address: yingfang.zhou@abdn.ac.uk (Y. Zhou).

or morphologies (Waite et al., 2009; Malagar et al., 2019; Chaouachi et al., 2015; Sahoo et al., 2018a; Dai et al., 2012; Helgerud et al., 1999). The commonly discussed hydrate morphologies include pore-filling (or pore-floating), pore-bridging (or load-bearing), and cementation. The pore-filling habit is normally defined as hydrate that disperses in the pore space but not bonds adjacent solid grains. It is found that pore-filling hydrate mainly affects the stiffness of pore fluids so that the effective elastic properties of the hydrate-bearing sediment are less influenced (Waite et al., 2009; Dai et al., 2012; Helgerud et al., 1999; Berge et al., 1999; Sahoo et al., 2018a). The load-bearing morphology is formed after hydrate particles coalesce and then bridge adjacent solid grains. The load-bearing hydrate is often found when hydrate saturation reaches 25%–40% (Waite et al., 2009; Sahoo et al., 2018a). From the mechanical point of view, the load-bearing hydrate can support the granular skeleton and resist loads, such that the hydrate-bearing sediments can be greatly stiffened by the presence of hydrate (Waite et al., 2009; Berge et al., 1999). Cementation morphology occurs when gas hydrate is formed at grain contact points, and it can enhance the stiffness of hydrate-bearing sediments significantly even with only a few hydrate particles (Waite et al., 2009; Sahoo et al., 2018a). The cementation morphology is more likely to occur during hydrate formation under excess-gas conditions (Waite et al., 2009; Dai et al., 2012; Priest et al., 2005).

As determining the relation of hydrate saturation and elastic properties is hampered by the complex hydrate morphology and the lack of in-situ hydrate-bearing cores, some empirical models have been established and widely used, such as the time-average equation (Wyllie et al., 1958), Wood's equation (Wood, 1960), and weighted equation (Lee et al., 1996). These analytical models provide fast estimations of the relationship between elastic moduli and elastic wave velocities and hydrate saturation, but they fail to capture the complex fluids-solid-hydrate spatial distribution in actual hydrate-bearing sediments (Ren et al., 2020). Some more physically-based models were also developed, such as Biot-Gassmann theory (BGT) (Lee, 2002a,b), Biot-Gassmann theory modified by Lee (BGTL) (Lee, 2002b), and three-phase effective medium theory (Helgerud et al., 1999), but they usually contain some parameters that are difficult to determine.

In addition to the lab measurements and analytical models, supported with the most recent advanced imaging techniques, a powerful numerical tool, the finite element method, has been adopted to probe the stress field within a specific domain for a given set of constraints (Lin et al., 2019; Huaimin et al., 2018). Previous studies have demonstrated the application of the FEM in predicting the effective elastic moduli and elastic wave propagation through random composites and porous mediums (Madadi et al., 2009; Arns et al., 2002; Faisal et al., 2017; Jing and Hudson, 2002; Andr a et al., 2013a; Dvorkin et al., 2011). The FEM includes two types, dynamic FEM and static FEM. The main difference between these two types of FEMs lies in that the static FEM does not account for non-linear cases in which: a) the stress-strain relation is non-linear (or yield stress occurs) so that the modulus of the component is strain-dependent; or b) large strains and/or deformation appears, which changes the global geometry of the domain (Andr a et al., 2013a). As for the prediction of elastic moduli and elastic wave velocities in hydrate-bearing rocks, the static FEM is often used. But due to the difficulty of obtaining high-resolution images of hydrate-bearing rocks, in most studies, the hydrate phase is introduced into a hydrate-free rock model through a mathematical morphology algorithm that simulates the growth and distribution of gas hydrate (Lin et al., 2019; Huaimin et al., 2018; Liu et al., 2020; Dong et al., 2021). However, this way of involving the hydrate phase cannot precisely capture the complex natures of hydrate distribution in the porous medium. Therefore, limited by the lack of precise digital information of hydrate-bearing rocks, the investigation of elastic moduli and elastic wave velocities through pore-scale numerical methods is still very rare.

In this study, we constructed a series of 3-D hydrate-bearing models with a wide hydrate saturation range based on the 4-D high-resolution

images of a synthetic hydrate-bearing sample. Then we investigated the elastic moduli and elastic wave velocities of the model and their relationship to the hydrate saturation and hydrate morphology through numerical simulations. Based on the simulated results, we proposed an empirical model that weights Wood's equation and Voigt upper bound. The model applies fast and trustworthy estimations of both compressional and shear wave velocities of hydrate-bearing sediments including free gas. Comparisons with some documented laboratory data validated the application of this analytical model.

2. Methodology

2.1. Sample and image process

The 4D high-resolution images of fluids-solid-hydrate distribution during the hydrate formation process were obtained through SRXCT (Sahoo et al., 2018a). In their work, a core sample (porosity = 35%) was made of Leighton Buzzard sands with a mean grain size of 100 μm ($d_{50} = 100 \mu\text{m}$). The core was saturated with 3.5 wt% brine to reach an initial brine saturation of 90%, and thus the subsequent hydrate formation would start under excess-water conditions. The entire system was then left under vacuum conditions for the pore fluids to favour a homogeneous distribution. Methane gas was then injected and a methane pressure of 10 MPa was achieved. A rigid confinement was provided to the system by a pressure cell made of polyetheretherketone (PEEK). The system was then cooled to 5 $^{\circ}\text{C}$ for hydrate formation. During the hydrate formation process, the SRXCT scanned the sample at resolutions of 1.625, 0.625 and 0.325 μm . In this work, the 3D images scanned at 16 h 42 m (1626 \times 1340 \times 300 pixels), 23 h 30 m (1830 \times 1788 \times 500 pixels), and 45 h 10 m (1810 \times 1838 \times 500 pixels) were collected since they were found to best describe the key hydrate formation process (Sahoo et al., 2018a), as shown in Fig. 1. Their resolutions are 0.625 μm , 0.325 μm , and 0.325 μm , respectively.

De-noising and segmentation processes were implemented to the 3D images. Some noises might exist in the raw images, which shades essential details of the core sample, and hence a proper treatment of noise reduction is necessary (Andr a et al., 2013b). Sell et al. (2016) applied different de-noising filters to reduce noises in hydrate-bearing images obtained by SRXCT and concluded that the performance of the non-local means filter and anisotropic diffusion filter was better than others. In this work, a non-local means de-noising plugin in the open-source image processing software, ImageJ, was applied to our datasets for noise reduction (Buades et al., 2011; Darbon et al., 2008). Furthermore, properly segmenting rock images into different phases is critical as it directly affects the volume fraction of each phase in the model, which is one of the main sources of uncertainties in numerical simulations (Andr a et al., 2013b). The most commonly used thresholding method is the global thresholding method (Iassonov et al., 2009). As the greyscale value in CT images is related to the density of constituents, ideally there will be four peaks in the greyscale histogram, and these peaks represent gas ($\sim 90 \text{ kg/m}^3$), hydrate ($\sim 925 \text{ kg/m}^3$), water ($\sim 1035 \text{ kg/m}^3$), and sand ($\sim 2650 \text{ kg/m}^3$), respectively (He et al., 2018; Jin et al., 2006). Correspondingly, the thresholding values will be set at the valley between two peaks. However, it is difficult to distinguish hydrate from water in some low-resolution models due to the low-density contrast between hydrate and water (Jin et al., 2006; Yang et al., 2015). In this work, benefiting from the high resolution, we found a clear separation between the hydrate and water phases, as shown in Fig. 2. A global thresholding segmentation method was then used to segment the system into four phases, and the segmented models can be seen in Fig. 1. The volume fraction of each component and porosity were then calculated, as presented in Table 1.

Additionally, the resolutions of original images were reduced by resampling the voxel sizes to save the time spent in numerical simulations. As the original resolutions were very high, subsequent numerical simulations on these images would suffer from the computing cost.

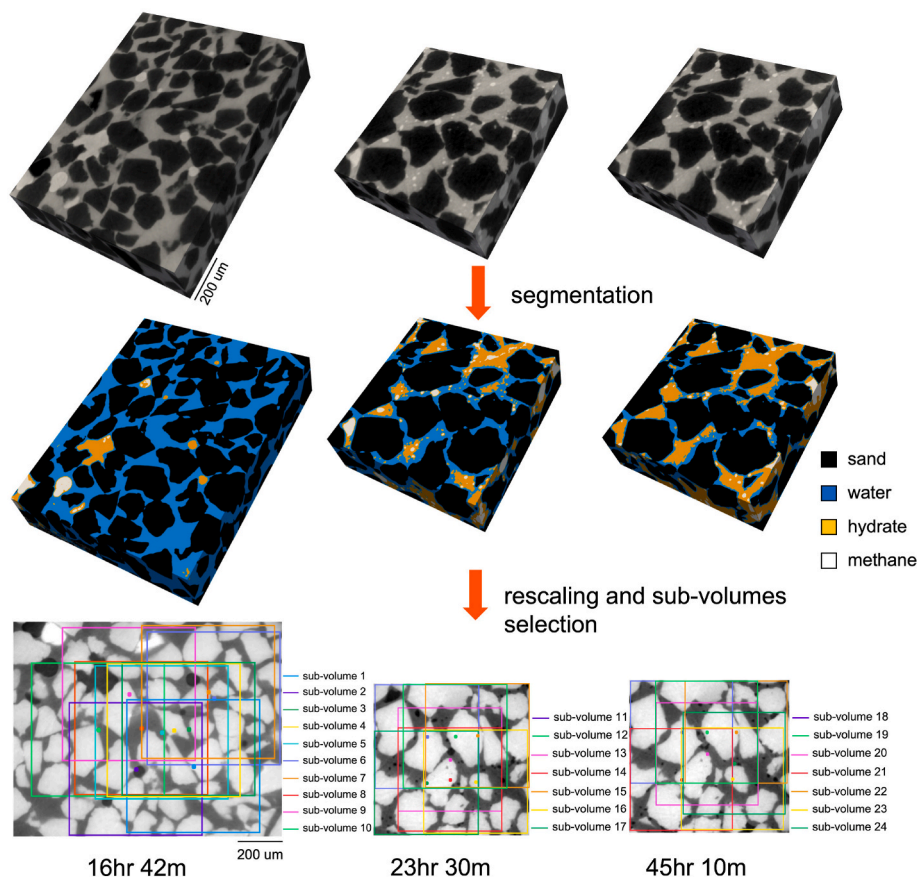


Fig. 1. Imaging processes in this work, including segmentation, rescaling and sub-volume extraction.

Therefore, the models were rescaled in ImageJ, through a bicubic interpolation algorithm (Catmull-Rom interpolation) proposed by Burger and Burge (2016). After some sensitivity tests, we reduced the resolution of images at 16hr 42 m twofold down to $1.25\ \mu\text{m}$, and the resolutions of images at both 23hr 30 m and 45hr 10 m quadruply to $1.3\ \mu\text{m}$. A typical comparison between original image and resampled image is depicted in Fig. 3. Consequently, the sizes of 3D images at 16hr 42 m, 23hr 30 m, and 45hr 10 m become $813 \times 670 \times 150$, $458 \times 447 \times 125$, and $453 \times 460 \times 125$, respectively. The porosity and volume fraction of different phases of the rescaled models were calculated, and the results are listed in Table 1. Compared with the original models, porosities, phase volume fractions, and saturations in rescaled models slightly changed by $-0.06 \sim -0.11\%$, $-0.25 \sim 0.95\%$, and $-2.54 \sim 2.69\%$, respectively.

We first determined the Representative Elementary Volumes (REV) of the segmented and rescaled high resolution hydrate-fluids-rock images, which will be used as input to investigate the effective elastic moduli and elastic wave velocities. REV is defined as the minimum volume beyond which properties sustain constant (Faisal et al., 2017). These characteristics include porosity (Rozenbaum and du Roscoat, 2014), water saturation (Costanza-Robinson et al., 2011), tortuosity (Borges et al., 2018), average pore and throat volumes (Yio et al., 2017), and fractal dimension (Wu et al., 2019), among which the porosity is the most commonly used parameter to determine the REV. In this work, we followed the same approach proposed by Wu et al. (2019) to use porosity to obtain the REV of the hydrate-bearing images. As shown in Fig. 4, the centre point of the rock images is selected to locate the position of the first cubic. The size of the centre cubic rock image is then incremented gradually, and the porosity of each cubic is computed. As displayed in Fig. 5, the calculated porosities of the generated 3D hydrate bearing images are presented as a function of image size. REVs of images

at 16hr 42 m, 23hr 30 m, and 45hr 10 m are $250 \times 250 \times 150$, $300 \times 300 \times 100$, and $300 \times 300 \times 100$, with corresponding physical volumes of $1.8e7\ \mu\text{m}^3$, $2.0e7\ \mu\text{m}^3$, and $2.0e7\ \mu\text{m}^3$, respectively. It is noted that the porosity in Fig. 5 (a) becomes stable at around 35% when the domain size reaches $250 \times 250 \times 150$ (corresponds to a physical volume of $1.8e7\ \mu\text{m}^3$). In Fig. 5 (b) and Fig. 5 (c), the porosity remains constant when the volume size reaches $300 \times 300 \times 100$ (corresponds to a physical volume of $2.0e7\ \mu\text{m}^3$). Hence, the REV of the three cases is close in physical size. In this work, we chose a slightly larger volume ($400 \times 400 \times 150$) as its REV in Fig. 5 (a) (Fig. 5 (a) is large enough to have a bigger REV) to avoid any uncertainty resulting from local heterogeneity.

Finally, we followed the hydrate-bearing model constructing method proposed by Chen et al. (2018), to develop a total of 24 hydrate-bearing with REV sizes by cropping original hydrate-bearing images. The locations of these sub-volumes are shown in Fig. 1. Sub-volumes 1 ~10 were extracted from images at 16hr 42 m, sub-volumes 11 ~17 were cropped from images at 23hr 30 m, and sub-volumes 18 ~24 were obtained from images at 45hr 10 m, respectively. The porosity and saturation information of these sub-volumes are listed in Table 2. The hydrate saturation of these sub-volumes ranges from 1.24 to 56.93%. The porosity fluctuates between 34.32% and 37.01%, with a maximum difference of 2.69%. Meanwhile, a set of hydrate-free models were created by duplicating these sub-volumes and treating the hydrate phase as water.

2.2. Simulation of elastic properties for hydrate-bearing rocks

To calculate effective elastic moduli and elastic wave velocities of hydrate-bearing models, the static finite element method (FEM) for linear elasticity proposed by Garboczi and Day (1995) is implemented in this work. The essence of the static FEM for linear elasticity is to seek the solution of a variational formulation of the linear elastic equations by

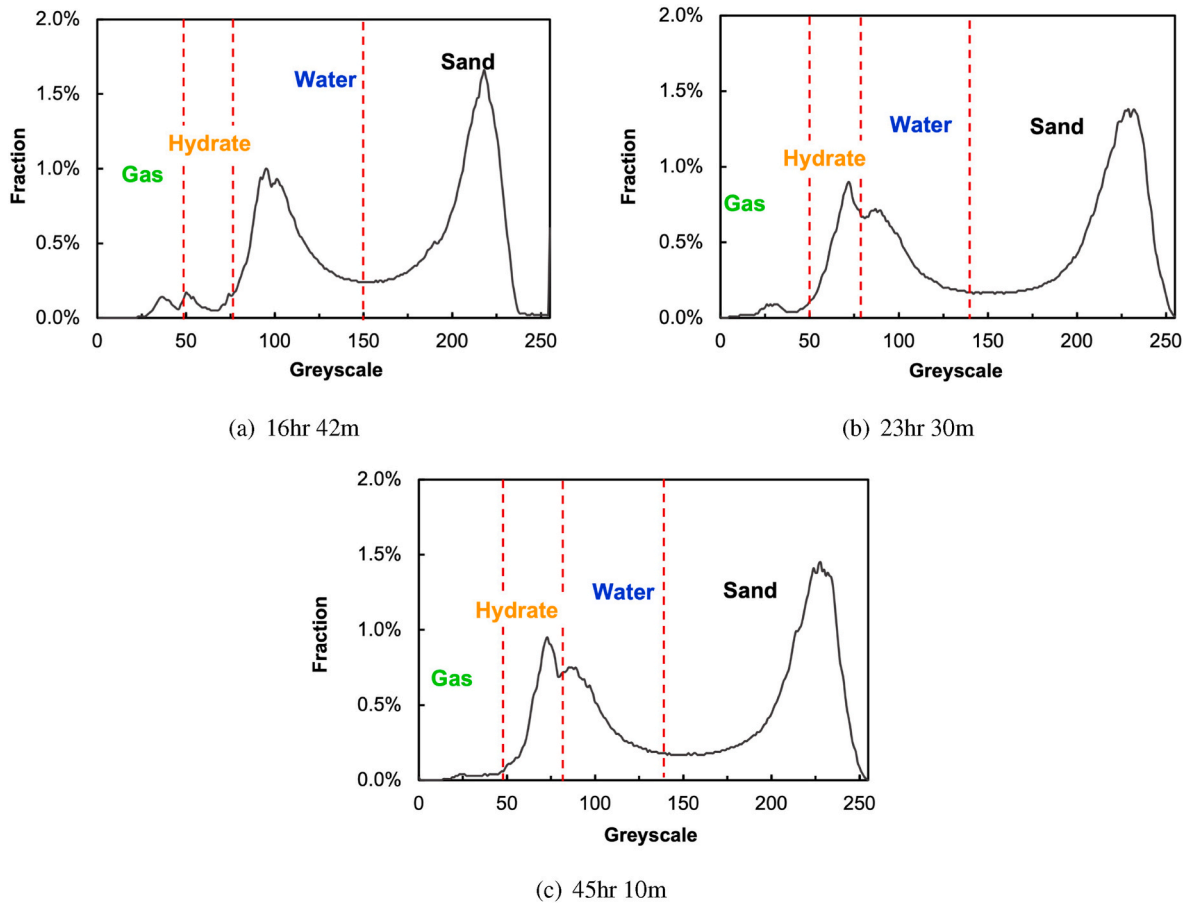


Fig. 2. Selection of global thresholding values in three datasets. Even though the hydrate and water overlapped, four greyscale peaks are still clearly presenting, which is helpful for thresholding.

Table 1
Porosity, phase volume fraction and saturation of original and rescaled models.

Models and cubic size	Porosity (%)	Volume fraction (%)				Saturation (%)		
		Sand	Brine	Hydrate	Gas	Brine	Hydrate	Gas
16hr 42min (1626 × 1340 × 300)	36.08	63.92	32.90	2.07	1.11	91.20	5.73	3.07
16hr 42min (813 × 670 × 150)	36.02	63.98	32.87	2.07	1.08	91.26	5.74	3.00
23hr 30min (1830 × 1788 × 500)	35.82	64.18	20.48	12.84	2.50	57.18	35.84	6.98
23hr 30min (458 × 447 × 125)	35.71	64.29	21.38	11.89	2.44	59.87	33.30	6.83
45hr 10min (1810 × 1838 × 500)	35.87	64.13	15.25	18.81	1.81	42.50	52.43	5.07
45hr 10min (453 × 460 × 125)	35.76	64.24	15.45	18.56	1.75	43.19	51.90	4.91

minimising the elastic energy with an iterative solver, such as the conjugate gradient method (Arns et al., 2002). The FEM algorithm used in this work is feasible for structured grid systems. Therefore, each pixel in digital images is treated as a trilinear finite element in the FEM, and thus the FEM can be directly applied to lattice digital models. Benefiting from the high resolution of the images used in this work, the structured grids can capture the complex pore space. Strain loadings are applied to the model to yield elastic deformation. Finally, the deformation field of the applied strain conditions is solved, and the effective elastic moduli are computed by the average stress and strain.

Practically in this work, to calculate effective elastic moduli of hydrate-bearing models, we first assign the bulk and shear modulus of each constituent to the model and each element (as listed in Table 3).

The periodic boundary condition, implying that the stresses and displacements at the nodes on one edge of the medium must be identical to the corresponding nodes on the opposite edge, was applied in the finite element method simulation to avoid any boundary effect resulting

from extra stress. Furthermore, six macro strains are applied (see Fig. 6), and six independent Finite element simulations are thus undertaken to solve for stress and displacement distributions of the six applied constant strains. The elastic displacements in each finite element are found, and thus stresses and strains in each element. Averaging the elemental stresses and strains over the entire simulation domain results in six macro stresses. Each strain constraint will yield a vector of six macro stresses. In total, six strain conditions will lead to 36 macro stresses. A stiffness tensor (in Voigt notation), C_{ijkl} is used in FEM to collect all the 36 components generated by these six macro strains in one matrix (Madadi et al. 2009). Inside the matrix, each macro strain contributes to a specific row in the matrix. The final form of the stiffness tensor is:

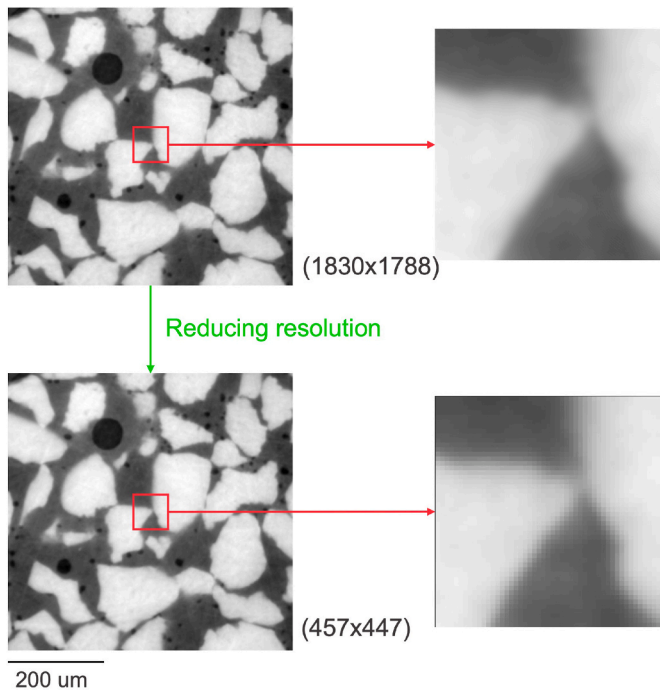


Fig. 3. Contrast between original image with resolution of 0.325 μm and resampled image with resolution of 1.3 μm. The boundary between phases becomes unclear in resampled image.

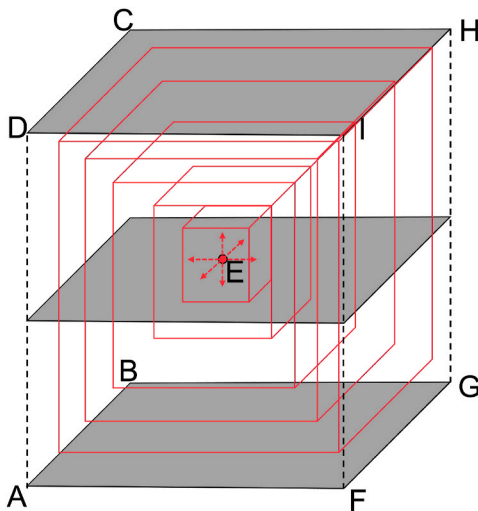


Fig. 4. The determination of the REV in a 3D model. Taking centre point E as the common centre of the cubics, the porosity is calculated after increasing the cubic size.

$$C_{ijkl} = \begin{Bmatrix} C_{11} & C_{12} & C_{13} & C_{14} & C_{15} & C_{16} \\ C_{21} & C_{22} & C_{23} & C_{24} & C_{25} & C_{26} \\ C_{31} & C_{32} & C_{33} & C_{34} & C_{35} & C_{36} \\ C_{41} & C_{42} & C_{43} & C_{44} & C_{45} & C_{46} \\ C_{51} & C_{52} & C_{53} & C_{54} & C_{55} & C_{56} \\ C_{61} & C_{62} & C_{63} & C_{64} & C_{65} & C_{66} \end{Bmatrix} \quad (1)$$

where 1 = xx, 2 = yy, 3 = zz, 4 = xz, 5 = yz, and 6 = xy. Finally, we analytically average the stiffness tensor over the Euler angles, which leads to a solution of effective bulk and shear modulus:

$$\begin{aligned} (C_{11})_{avg} &= \frac{1}{3}(C_{11} + C_{22} + C_{33}) \\ (C_{44})_{avg} &= \frac{1}{3}(C_{44} + C_{55} + C_{66}) \\ (C_{12})_{avg} &= \frac{1}{3}(C_{12} + C_{13} + C_{23}) \\ \langle C_{11} \rangle &= \frac{3}{5}(C_{11})_{avg} + \frac{2}{5}(C_{12})_{avg} \\ G_{eff} &= \frac{1}{5}[(C_{11})_{avg} - (C_{12})_{avg} + 3(C_{44})_{avg}] \\ K_{eff} &= \langle C_{11} \rangle - \frac{4}{3}G_{eff} \end{aligned} \quad (2)$$

where K_{eff} and G_{eff} are the effective bulk and shear modulus. With the effective bulk and shear modulus, we can calculate the compressional and shear wave velocity of this model by:

$$V_p = \sqrt{\frac{K_{eff} + \frac{4}{3}G_{eff}}{\rho_{eff}}} \text{ and } V_s = \sqrt{\frac{G_{eff}}{\rho_{eff}}} \quad (3)$$

where ρ_{eff} denotes the effective density of the microstructure. V_p and V_s are the compressional and shear wave velocity.

3. Results and discussion

3.1. Hydrate distribution in pore space

Fig. 7 shows 3D views of critical findings of hydrate distributions with the increase of the hydrate saturations. At a lower hydrate saturation (Fig. 7 (a)), hydrate forms around gas bubbles floating in the pore space, resulting in the formation of hydrate shells. This is because that the hydrate formation consumes both water and gas, thus hydrate tends to nucleate at the gas-water interface. As gas bubbles and gas pockets are rich sources of free gas, hydrate will preferentially form around them (Sahoo et al., 2018a). Additionally, some hydrate blocks can form when hydrate saturation is low (Fig. 7 (b)). Water separates the hydrate and solid grains, such that hydrate shells and hydrate blocks are floating in the pore space. Finally, when a significant amount of hydrate clusters coalesce, the hydrate framework forms, which blocks the most pore space (Fig. 7 (c)). Some scattered free gas bubbles remain in the hydrate framework even when hydrate saturation reaches 56.93%. This is because that the formation of hydrate shells around gas bubbles can inhibit the water outside from consuming inner gas to create new gas hydrates (Sahoo et al., 2018a). Furthermore, water films are always present that enclose hydrate solid, which separates the matrix and hydrate.

A more detailed 2D view of the evolution of hydrate with hydrate saturations is depicted in Fig. 8. As shown in this figure, the hydrate pore habit is evolving with hydrate saturation and can be divided into three stages. In the first stage, gas hydrate forms around gas bubbles and gas pockets, resulting in the formation of hydrate shells and hydrate blocks when hydrate saturation is very low (see Fig. 8 (a) ~ (d)). In the second stage, a massive amount of hydrate is present in the centre of the pore space, exhibiting a pore-filling hydrate morphology (see Fig. 8 (e) ~ (h)). In the third stage, the hydrate clusters coalesce, forming large hydrate blocks that eventually occupies most of the pore space (see Fig. 8 (i) ~ (l)). In addition, a thin water film is present between hydrate and solid surface even when hydrate saturation is very high (as highlighted in Fig. 8 (j)). Also, some gas bubbles can remain inside the hydrate chunks (see Fig. 8 (l)).

3.2. Elastic moduli and elastic wave velocities of hydrate-bearing models

Fig. 9 depicts the elastic wave velocities and effective elastic moduli of hydrate-bearing models and hydrate-free models. As shown in this

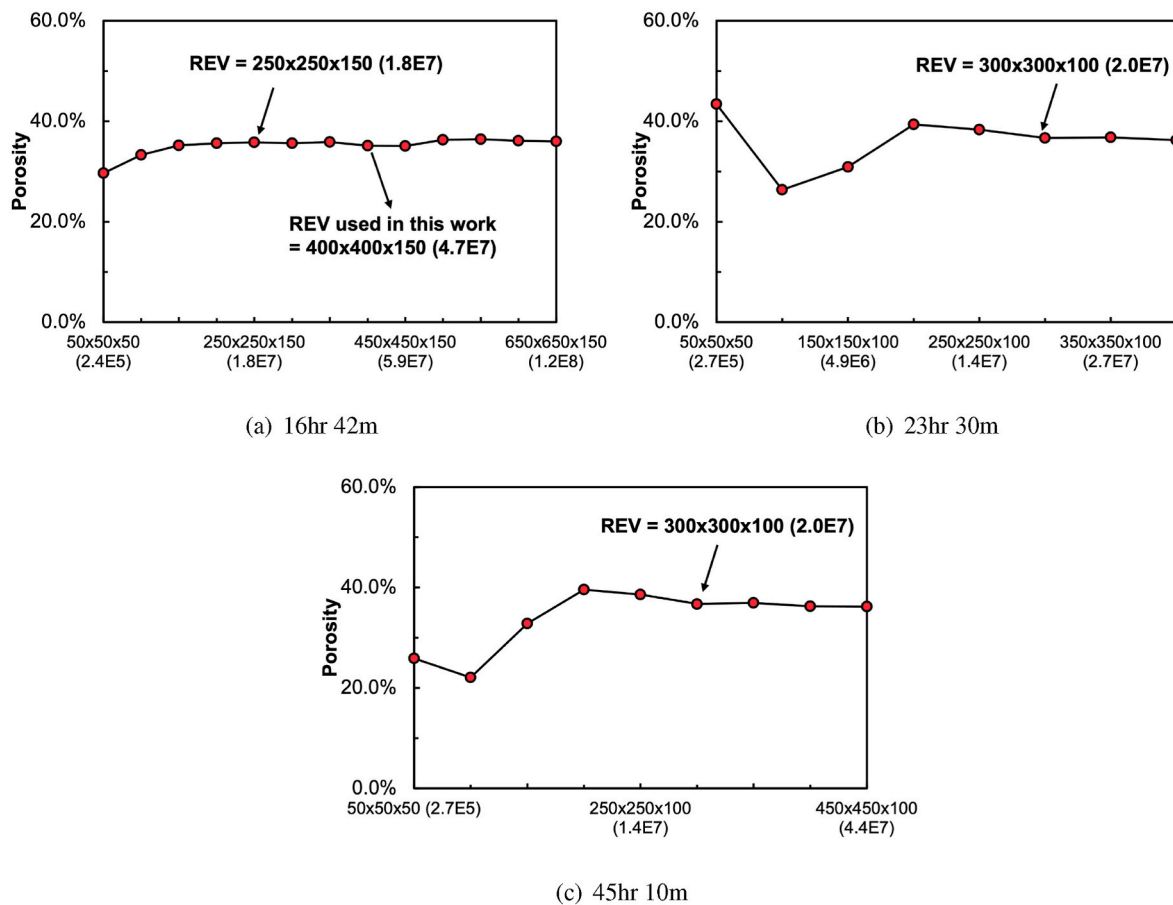


Fig. 5. REV determination of three hydrate-bearing models in this work. Values in brackets on X-axis are physical volume in μm^3 . The REV of images at 16hr 42m, 23hr 30m, and 45hr 10m are $250 \times 250 \times 150$, $300 \times 300 \times 100$, and $300 \times 300 \times 100$, respectively. It is noted that a bigger REV is set at $400 \times 400 \times 150$ in (a).

Table 2
Porosity and fluid saturations of 24 sub-volumes.

Label	Porosity (%)	S_g (%)	S_h (%)	S_w (%)	Label	Porosity (%)	S_g (%)	S_h (%)	S_w (%)
1	34.97	0.71	1.24	98.05	13	36.63	7.40	30.16	62.44
2	36.08	1.10	1.40	97.50	14	37.01	6.33	31.87	61.80
3	34.95	1.17	1.56	97.28	15	35.37	8.44	35.12	56.44
4	35.01	1.31	1.83	96.85	16	35.49	5.53	36.68	57.79
5	35.11	1.43	2.58	95.99	17	35.07	5.34	38.18	56.48
6	35.68	1.87	3.97	94.16	18	35.09	4.50	45.56	49.94
7	36.01	1.98	4.39	93.63	19	36.00	5.06	49.38	45.55
8	35.14	1.61	5.79	92.60	20	36.74	4.83	51.09	44.09
9	36.03	2.64	7.76	89.60	21	36.85	4.07	52.76	43.17
10	34.67	2.46	8.44	89.10	22	35.34	4.71	54.22	41.07
11	34.32	6.73	23.27	70.00	23	35.11	4.13	55.91	39.96
12	35.52	7.70	29.31	62.99	24	35.83	3.20	56.93	39.87

Table 3
Input parameters of different components.

	$\rho(\text{kg}/\text{m}^3)$	$K(\text{GPa})$	$G(\text{GPa})$
Sand	2650 ^a	36 ^a	44.54 ^a
Hydrate (5 MPa, 273 K)	925 ^a	7.9 ^a	3.23 ^a
Brine	1035	2.3 ^b	0 ^b
Methane (10 MPa, 273 K)	90 ^c	0.015 ^c	0 ^c

^a (Sahoo et al., 2018a).

^b (Millero et al., 1980).

^c (Waite et al., 2009).

figure, the hydrate-bearing models have higher elastic wave velocities and elastic moduli than the hydrate-free models because the gas hydrate stiffens the host sediments. Elastic wave velocities and elastic moduli of hydrate-bearing models all increase with higher hydrate saturation, which makes the difference between hydrate-bearing models and hydrate-free models greater. Notably, for the shear wave velocity and shear modulus, the hydrate-bearing and hydrate-free models overlap when hydrate saturation is less than 10%. While the difference in compressional wave velocity and bulk modulus between hydrate-bearing and hydrate-free models is quite high when hydrate saturation is very low. In addition, the elastic moduli and elastic wave velocities of hydrate-free models are not stable since the geometry of these 24 sub-volumes are different. But since this difference is very low compared to it caused by the increase of hydrate saturation, the influence of

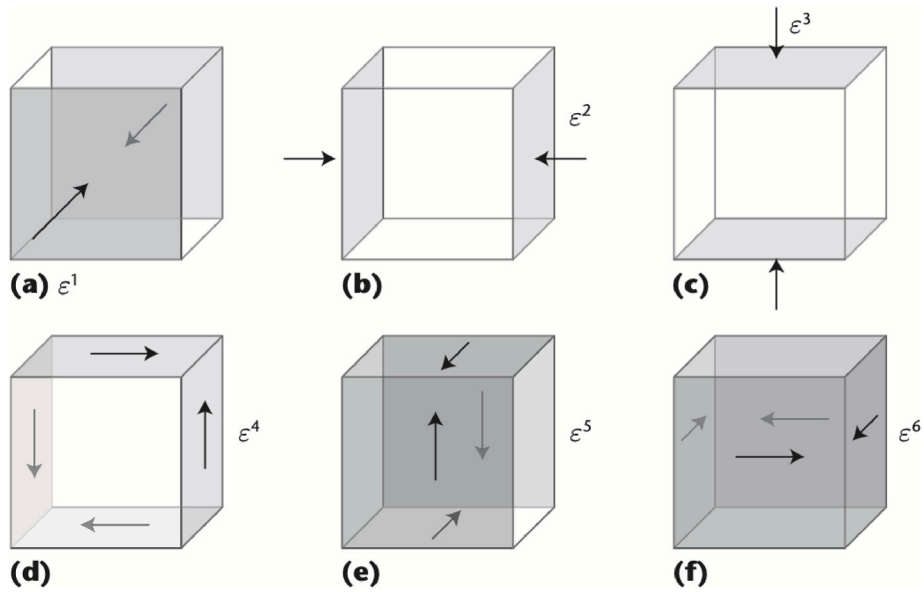


Fig. 6. Six strain loading conditions applied in the FEM simulations. (a)–(c) are the uniaxial strain loadings and (d)–(f) are shear strain loadings. Taken from Madadi et al. (2009).

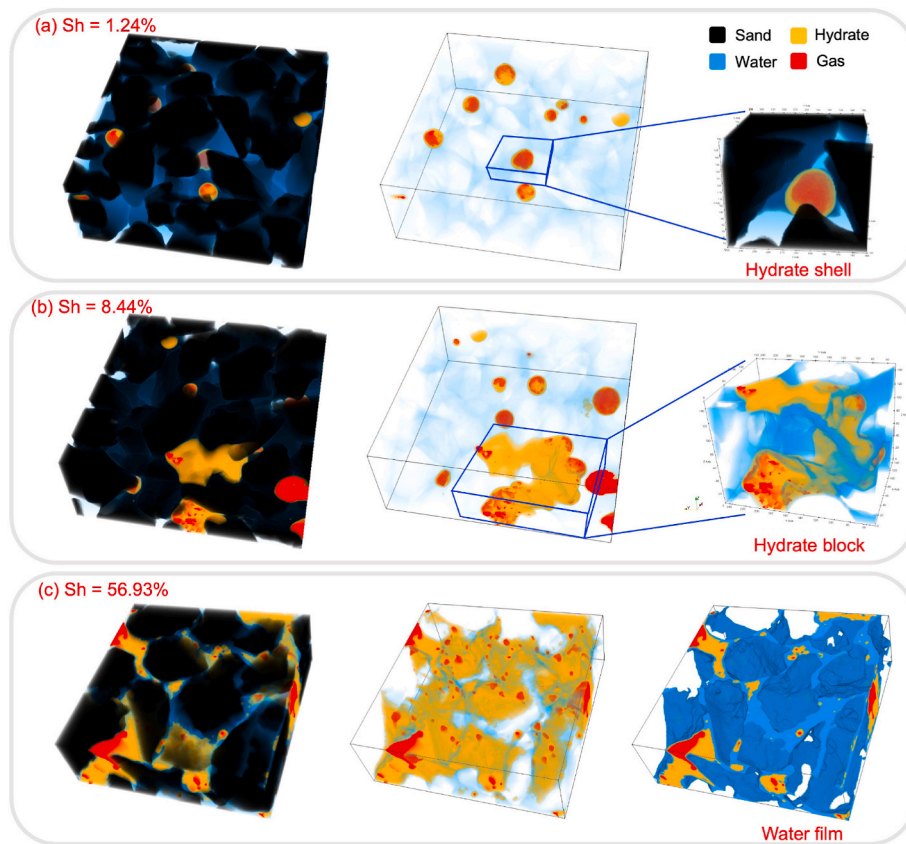


Fig. 7. 3D views of gas hydrate distribution in the pore space at hydrate saturation of (a) 1.24%, (b) 8.44%, and (c) 56.93%. Images in the left column are segmented 3D images. The middle images are highlighted views of hydrate distributions. Images on the right illustrate hydrate shell, hydrate block, and water film, respectively.

different geometry on the elastic moduli and elastic wave velocities of the hydrate-bearing models can be neglected.

Fig. 10 shows the difference in bulk modulus, shear modulus, compressional and shear wave velocities between hydrate-bearing and hydrate-free models. The point (0, 0) is fixed in both figures since the hydrate-bearing model becomes identical to the hydrate-free model

when hydrate saturation equals 0.

As shown in Fig. 10 (a) and (b), the change in elastic moduli and elastic wave velocities are similar, as elastic wave velocities are positively related. ΔK , ΔG , ΔV_p and ΔV_s all increase with higher hydrate saturation. According to the slope of the trend line presenting in bulk modulus and compressional wave velocity, the results can be classified

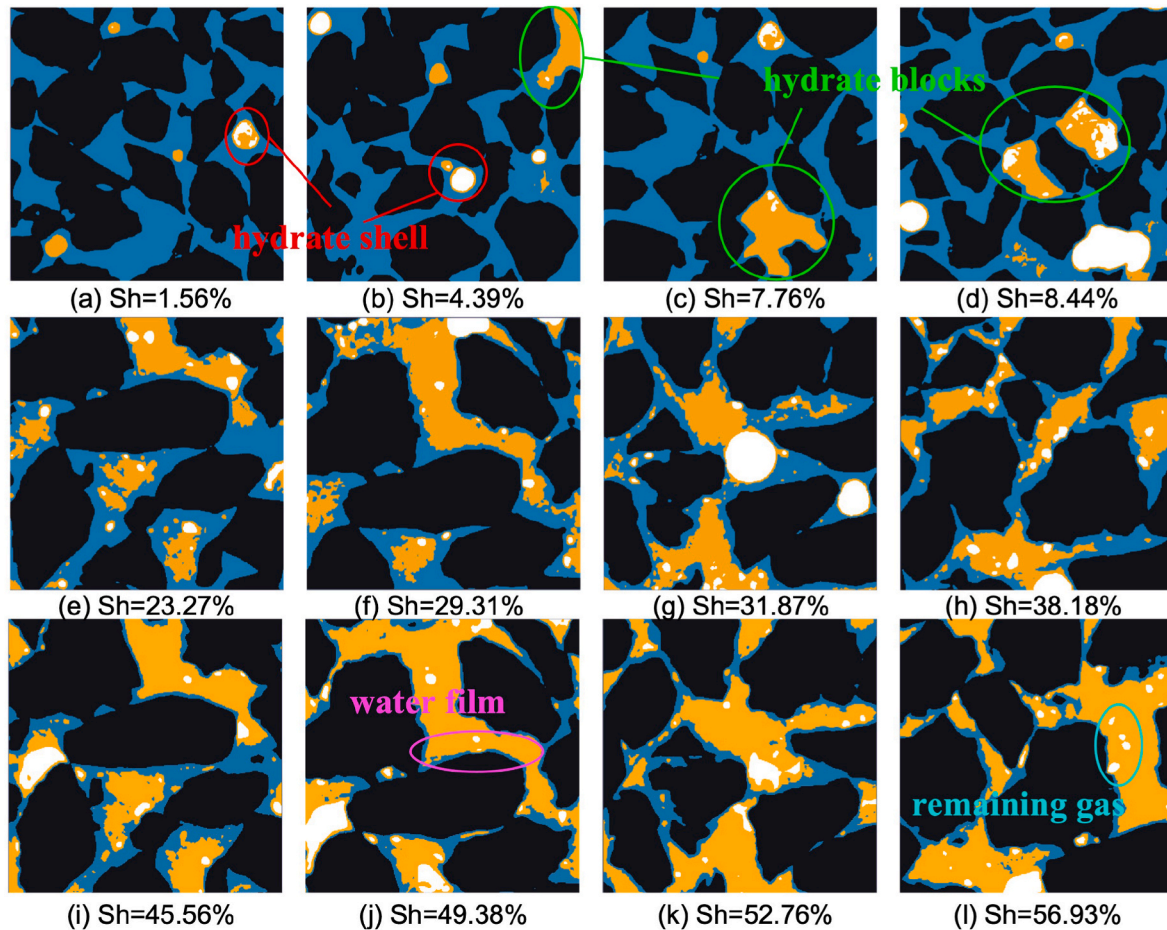


Fig. 8. 2D views of gas hydrate distribution in the pore space at different hydrate saturations. Black denotes the sand, blue the brine, yellow the hydrate, and white the gas. Some notable features, including hydrate shells, hydrate blocks, water film, and remaining gas are highlighted. (For interpretation of the references to colour in this figure legend, the reader is referred to the Web version of this article.)

into four stages. They are an initial increase ($S_h = 0 \sim 5\%$), a flat rise ($S_h = 5 \sim 35\%$), a steeper growth ($S_h = 35 \sim 50\%$), and a plateau ($S_h > 50\%$).

Specifically, a sharp increase of both ΔK and ΔV_p occurs at low hydrate saturation. Some previous studies have reported similar findings when synthesising hydrate-bearing rock samples under excess-gas conditions (Waite et al., 2004, 2009; Dai et al., 2012; Priest et al., 2005, 2009; Xing et al., 2020). This is because that hydrate initially cements grain contacts and stiffens the host sediments. It is also suggested that this sharp increase of elastic modulus at small hydrate saturation could be triggered by the fact that the hydrate preferentially forms in some micro-fractures at the beginning of the hydrate formation process, which stiffens the host sediments remarkably (Sahoo et al., 2018a). However, in this work, we ascribe this sharp enhancement to the formation of hydrate shells and hydrate blocks. The existence of free gas will greatly reduce the compressional wave velocity, and the formation of hydrate shells can dampen this reduction (Lei et al., 2019). Hence, as hydrate preferentially forms around gas bubbles, it can cause a significant increase of bulk modulus and compressional wave velocity. Meanwhile, as observed from Fig. 8, some hydrates can form large chunks that locally block adjacent solid grains. This local block may also enhance host sediments stiffness. But no initial increase in shear modulus and shear wave velocity is identified. This is due to the water films that separate the hydrate and solid grains so that the shear modulus and shear wave velocity are less influenced.

Following is a flat rise in both elastic moduli and sound wave velocities that continues until hydrate saturation reaches around 35%. In

this period, a large amount of gas hydrate forms in the pore space and exhibits a dominant pore-filling morphology (Priest et al., 2005; Xing et al., 2020). As a majority of hydrate particles are floating in the pore space, they hardly enhance the stiffness of the host sediments.

A steeper increment occurs when hydrate saturation is higher than 35%. In this period, hydrate particles coalesce and form an inter-pore hydrate framework that interlocks with the solid grains. The rise in the growth rate of elastic moduli and elastic wave velocities marks a transition of hydrate morphology from pore-filling to load-bearing.

Finally, a plateau is reached when hydrate saturation exceeds 50%, indicating that hydrate framework blocks the pore space so that little hydrate will form due to lack of source of enough free gas and water.

3.3. Comparison with analytical modelling of elastic wave velocities

The simulated elastic wave velocities are compared with those calculated by the analytical models. Fig. 11 displays the contrast of compressional wave velocities obtained from the time-average equation (Wyllie et al., 1958) (see Appendix A.1), Wood's equation (Wood, 1960) (see Appendix A.2), and our simulation. As shown in Fig. 11 (a), both the Time-average and Wood's equation underestimate the compressional wave velocity, especially for Wood's equation that yields a significantly lower prediction. It is because both equations are sensitive to the lighter components. In Wood's equation, the gas phase term on the right side, f_g/K_g can be orders of magnitude higher than other terms. Though the gas phase term in the Time-average equation (f_g/V_g) has less influence, it can still be much higher than other terms. Meanwhile, as shown in

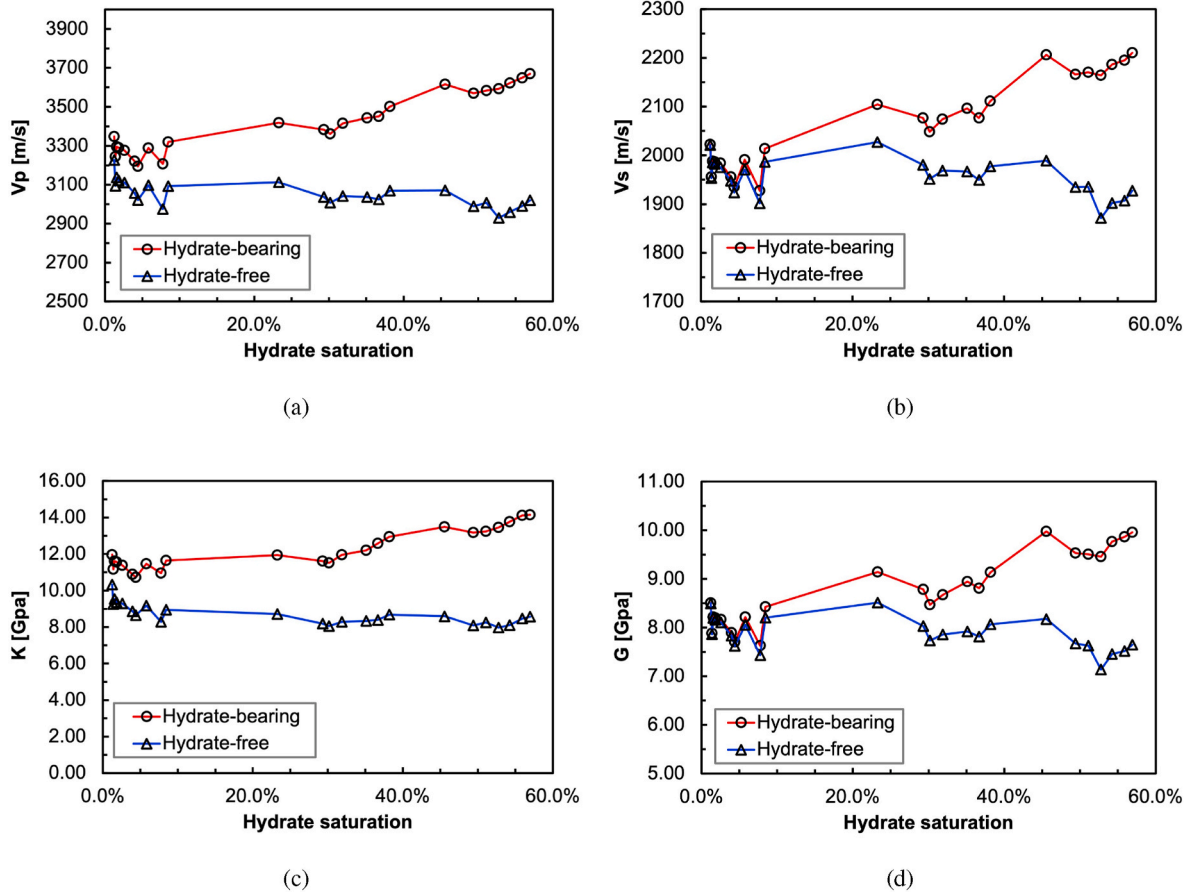


Fig. 9. Comparisons of elastic wave velocities and effective elastic moduli between hydrate-bearing models and hydrate-free models. (a) and (b) are compressional and shear wave velocity; (c) and (d) are effective bulk and shear modulus. Note that the elastic wave velocities and elastic moduli of hydrate-free models are not a function of hydrate saturation.

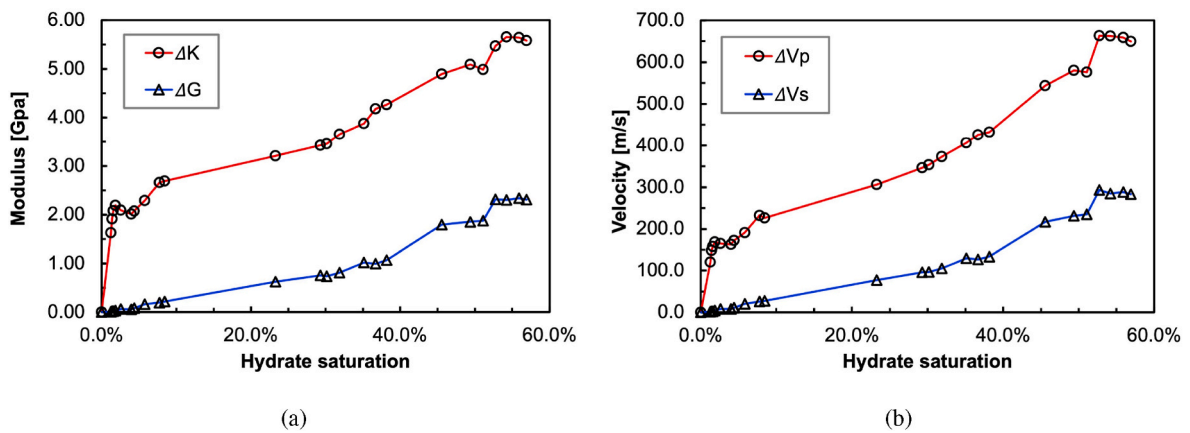


Fig. 10. The change in bulk and shear moduli, and elastic wave velocities with respect to hydrate saturation. The trend lines and their slopes are marked in both figures.

Fig. 11 (b), the compressional wave velocity computed by Wood's equation decreases at first and then increases, which is correlated with the trend of the gas volume fraction. It demonstrates that the gas concentration affects Wood's equation dramatically even though it is quite low in the hydrate-bearing models. Hence when involving the free gas phase, both Time-average and Wood's equation will underestimate the compressional wave velocity of hydrate-bearing sediments.

The simulated elastic wave velocities are then compared with the weighted equation (Lee et al., 1996; Lee and Collett, 2001) (see

Appendix A.3) and BGT model (Krief, 1990; Lee, 2002a) (see Appendix A.4). As depicted in Fig. 12, the simulated elastic wave velocities are within the BGT predictions (pore-filling and load-bearing case), indicating that the hydrate morphology is a mix of pore-filling and load-bearing morphology. However, when hydrate saturation is less than 30%, the simulated compressional wave velocity exceeds the BGT predictions. This is because that the BGT model cannot accurately capture the complex hydrate morphology when hydrate saturation is low. The BGT model assumes that the hydrate is homogeneously distributed

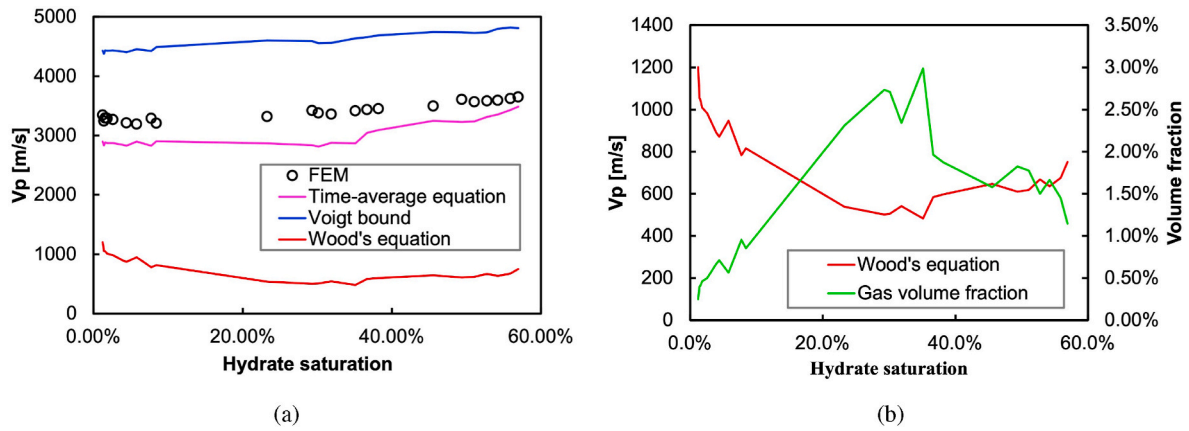


Fig. 11. (a) shows comparisons of compressional wave velocities obtained from the time-average equation, series equation, Wood's equation, and numerical simulation; (b) is the correlation between the compressional wave velocity computed by the Wood equation and the gas volume fraction changes.

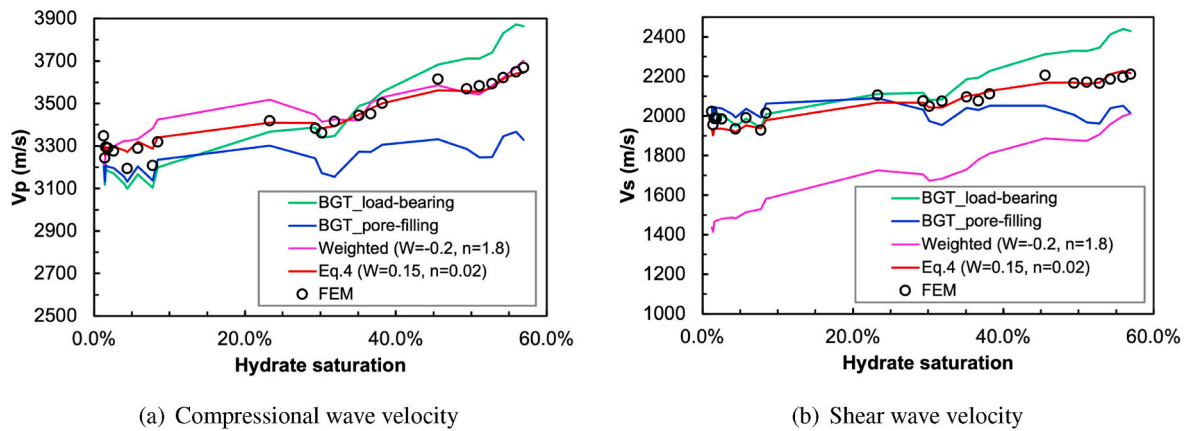


Fig. 12. Comparisons of elastic wave velocities obtained from the weighted equation by Lee, BGT of load-bearing and pore-filling case, equation (5), and numerical simulation.

as part of either the solid matrix (load-bearing case) or the fluid (pore-filling case). At a lower hydrate saturation, the volume fraction of hydrate dominates the magnitude of the elastic moduli and elastic wave velocities in the BGT model rather than hydrate morphology. Hence, when hydrate saturation is low, the elastic wave velocities will not change greatly. But in practice, hydrate shells and hydrate blocks can stiffen the host sediments. Thus the simulated elastic wave velocity is higher than the BGT predictions at a lower hydrate saturation.

Notably, the simulated shear wave velocities match the load-bearing case of BGT model calculations at lower hydrate saturations (see Fig. 12). It seems that the initial hydrate morphology tends to be load-bearing, which is contradictory to what has been found from Fig. 10. In addition, the shear wave velocity calculated by the pore-filling case was found to exceed the load-bearing case at low hydrate saturations. This abnormal feature is due to limitations inherent in the two different hydrate treatment methods of the BGT model. Taking the hydrate-bearing model (Label 8 in Table 2) as an example, the matrix bulk and shear modulus are calculated by Equation A.8, and they are 33.81 GPa and 37.67 GPa in load-bearing case. The matrix in the pore-filling case has only quartz, hence, the matrix bulk and shear modulus are the same as those of quartz, 36 GPa and 44.54 GPa. In the load-bearing case, treating the hydrate as part of the matrix reduces the porosity from 35.14% to 33.10%, while it is 35.14% in the pore-filling case. As a result, the effective bulk and shear modulus in the load-bearing case are 9.88 GPa and 8.17 GPa, while they are 9.81 GPa and 8.59 GPa in the pore-filling case. The bulk moduli of the two cases show no great difference, thus when calculating the elastic wave velocities using Equation

(3), the shear modulus dominates the result. The compressional and shear wave velocity are 3166 m/s and 1986 m/s in the load-bearing case, while in the pore-filling case, they are 3202 m/s and 2036 m/s. From this example, we can find that treating the hydrate as part of the matrix will significantly reduce the matrix stiffness, especially the shear modulus. Nonetheless, the porosity reduction brought by the hydrate treatment method can increase the rock stiffness. Therefore, at low hydrate saturations (less than around 15% in Fig. 12), the load-bearing case does not exceed the pore-filling case in which treating the hydrate as a fluid phase increases the stiffness of the fluid and thus the entire system.

The weighted equation can generate a reasonable compressional wave velocity after properly tuning the free parameters. As both Time-average and Wood's equation underestimate the compressional wave velocity, the weighting factor has to be negative to match the simulated results. In our case, a negative weighting factor of $W = -0.2$ is used in the weighted equation. In addition, the weighted equation yields shear wave velocities that are much lower than the simulated and the BGT modelling results.

3.4. An improved model for effective elastic wave velocities in hydrate-bearing sediments

In order to analytically calculate the effective elastic wave velocities when including free gas phase, we evoked a Voigt bound for elastic wave velocity replacing the Time-average equation in the weighted equation. The Voigt bound is used for predicting elastic moduli of the composite. It

assumes that all the components in the composite are arranged in series, thus it normally gives the maximum possible elastic moduli of the composite (Hill, 1963). We adapted the Voigt bound for calculating elastic wave velocities, which is expressed as

$$V_{p,s} = fV_{p,s}|_{gas} + fV_{p,s}|_{water} + fV_{p,s}|_{hydrate} + fV_{p,s}|_{solid} \quad (4)$$

where $V_{p,s}$ is either the compressional or shear wave velocity. In this equation, the product of the gas volume fraction and elastic wave velocity is much lower than the term of the stiffest components, and thus the influence of the gas phase on the elastic wave velocities is less prominent. As a result, the effective wave velocities are affected more by the stiffer components, so that this model can overestimate the wave velocities. As shown in Fig. 11, the compressional wave velocity calculated by equation (4) is much higher than the simulated results and other empirical modelling results.

Combining with Wood's equation, an updated weighted equation for predicting elastic wave velocities of the hydrate-bearing sediments considering the free gas phase is expressed as:

$$V_{p,s} = V_{p,s,1} W S_h^{\frac{n}{W}} + V_{p,s,3} (1 - W) \left[1 - W(1 - S_h)^{\frac{n}{W}} \right] \quad (5)$$

where $V_{p,s,1}$ is the wave velocity computed from Wood's equation, and $V_{p,s,3}$ is the wave velocity computed from equation (4). A lithification parameter n that controls the contribution of hydrate concentration to the lithification rate of the sediments is included in this weighted equation. Particularly, in calculating the shear wave velocity, Wood's equation yields a zero value, and the effective shear wave velocity is then determined only by the second term on the right side of equation (5).

The elastic wave velocities computed by equation (5) are shown in Fig. 12. Contrast to the previous weighted equation (Appendix A.3), equation (5) matches both compressional and shear wave velocity reasonably after finely tuning the weighting factor ($W = 0.15$ and $n = 0.2$).

Equation (5) was then used without free gas phase to match with experimental data proposed by Priest et al. (2005) (Fig. 13 (a)), Priest et al. (2009) (Fig. 13 (b)), Hu et al. (2010) (Fig. 13 (c)), and Chen et al. (2021) (Fig. 13 (d)). The elastic properties of different components in equation (5) came from the corresponding literatures. Priest et al. (2005) measured elastic wave velocities of thirteen sand specimens with different amount of hydrate formed by the 'ice-seeding' method (Fig. 13 (a)). As such the hydrate was formed under an excess-gas condition, and no remaining free water after the hydrate formation process was hypothesised. Therefore, the elastic wave velocities quickly increase at low hydrate saturations, which implies that hydrate cements sand contacts. Priest et al. (2009) also constructed hydrate-bearing sand specimens by excess-water condition and measured the elastic wave velocities (Fig. 13 (b)). In both cases, equation (5) yields V_p and V_s which are consistent with the measurement data. However the model works less adequately at low hydrate saturations in Fig. 13 (a), implying that the calculation of V_s by the model is more suitable in excess-water conditions.

The analytical model was further applied to a hydrate-bearing Mullite sample (Hu et al. (2010), Fig. 13 (c)) and hydrate-bearing sand sample with different methane fluxes (Chen et al. (2021), Fig. 13 (d)). We found a great consistency of both V_p and V_s between the model predictions and these laboratory measurements.

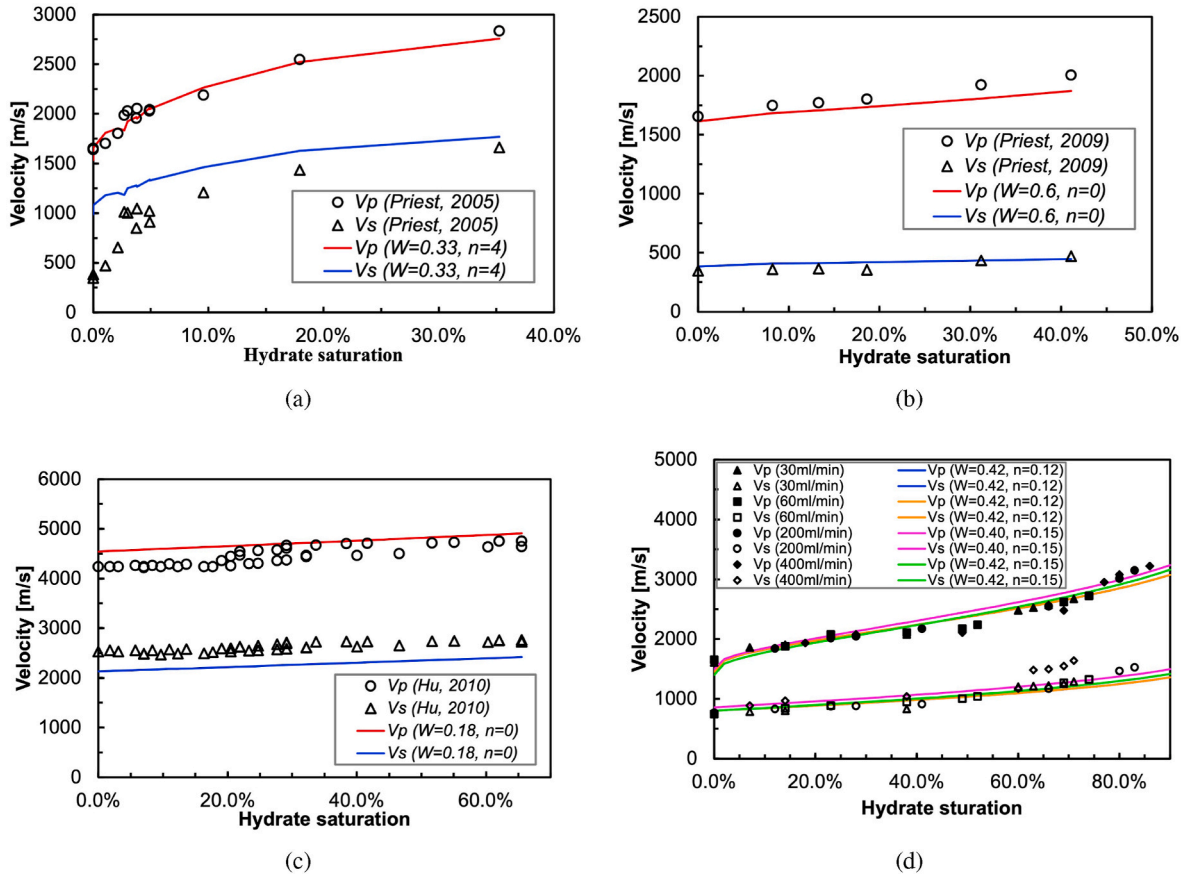


Fig. 13. Comparisons of elastic wave velocities predicted by equation (5) and experimental tests proposed by (a) Priest et al. (2005), (b) Priest et al. (2009), (c) Hu et al. (2010), and (d) measured velocities documented in Chen et al. (2021). The scattering open circles and squares represent the measured compressional and shear wave velocity, and lines denote the corresponding elastic wave velocities computed by equation (5).

4. Conclusions

The recent advanced imaging techniques make it possible to visualise the pore-scale hydrate morphology evolution in hydrate-bearing rocks. This study adopts the finite element method to simulate the in-situ stress and strain distribution in hydrate-bearing rock (under various hydrate saturations) at pore scale based on 4D high-resolution synchrotron radiation images. The effective elastic moduli and elastic wave velocities of hydrate-bearing models are calculated based on simulated stress and strain distributions at different stages during the hydrate formulation process. This allows us to investigate the influence of pore-scale hydrate morphology on geophysical properties, such as elastic wave velocities, and to formulate a more realistic geophysical function for better hydrate formulation evaluation.

The simulation results demonstrate the dependency of geophysical properties on pore-scale hydrate morphology under varied hydrate saturation conditions. Based on this work, a few key conclusions can be summarised as follows:

The dominant hydrate morphology experiences a transition from pore-filling morphology to load-bearing morphology and to interconnect hydrate framework at the hydrate formulation process. Hydrate nucleates around gas bubbles and gas pockets dispersed in the pore space at low hydrate saturation (smaller than 10%), forming hydrate shells and chunks that locally block adjacent pore space.

The formation of local hydrate blocks at low hydrate saturation can increase the bulk modulus and compressional wave velocity of the host sediments significantly. While the shear modulus and shear wave velocity are less affected due to the presence of water films that separate the hydrate and solid grains.

The existing time-average and Wood's equation underestimate the compressional wave velocity when considering the free gas phase. The weighted time-average and Wood's equation fail to predict shear wave velocity appropriately when involving the free gas.

The newly proposed Wood's and Voigt bound weighted equation was

first validated against laboratory-measured elastic wave velocity without gas, and it also demonstrates better estimations in both compressional and shear wave velocity.

In this work, we demonstrated the feasibility of constructing hydrate-bearing models with different hydrate saturations based on selecting sub-volumes of different locations and hydrate formation times. Although these hydrate-bearing models vary in porosity and are constructed from different locations, we constrained the change in porosity and drew our conclusions from elastic properties differences, which to the best extent diminishes the influence of varying porosity and domain locations. But an ideal attempt is to develop hydrate-bearing models based on digital images from the same location and different hydrate formation times during the hydrate formation process. This work is limited to hydrate formulation in unconsolidated sandy sediments, and hence a natural extension of this work is to look at the geophysical properties evolution in more complicated natural porous materials, such as consolidated sandstones, fine sandy sediments and fractured rocks, as well as hydrate dissolution process.

Declaration of competing interest

The authors declare that they have no known competing financial interests or personal relationships that could have appeared to influence the work reported in this paper.

Data availability

Data will be made available on request.

Acknowledgments

The financial support for this study was from PetroChina. We also thank S. K. Sahoo for sharing the high resolution 4D synchrotron radiation imaging data of hydrate formation.

Appendix A. Analytical models of elastic wave velocities

Appendix A.1. Time-average equation

In the time-average equation, different constituents are assumed in a parallel arrangement and the slowness (the inverse of the compressional wave velocity) is a weighted sum of the slowness of each constituent. The time-average equation is thought to be valid for mixtures of greater consolidation and rigidity, i.e., mixtures with low porosities (Lee et al., 1996; Nobes et al., 1986). Considering the free gas phase, the four-phase time-average equation is:

$$\frac{1}{V_p} = \frac{f}{V_p}|_{gas} + \frac{f}{V_p}|_{water} + \frac{f}{V_p}|_{hydrate} + \frac{f}{V_p}|_{solid} \quad (A.1)$$

where f denotes the volume fraction of each phase.

Appendix A.2. Wood's equation

Another empirical model for the compressional wave velocity is Wood's equation (Wood, 1960). Wood's equation is used in a fluid suspension or fluid mixture, and it is thus more applicable in systems with greater porosities, such that the solid phase breaks down into individual particles that are suspended in the fluid phase (Nobes et al., 1986). The bulk modulus of a four-phase hydrate-bearing sediment can be defined as:

$$\frac{1}{K_{eff}} = \frac{f}{K}|_{gas} + \frac{f}{K}|_{water} + \frac{f}{K}|_{hydrate} + \frac{f}{K}|_{solid} \quad (A.2)$$

as the system is treated as a fluid mixture, the compressional wave velocity is then calculated by:

$$V_p = \sqrt{\frac{K_{eff}}{\rho_{eff}}} \quad (A.3)$$

Appendix A.3. Weighted equation

Combining the time-average equation and Wood's equation by a weighting factor, a commonly used weighted equation was established (Lee et al., 1996; Lee and Collett, 2001), which is

$$\frac{1}{V_p} = \frac{W\varphi(1 - S_h)^n}{V_{p1}} + \frac{1 - W\varphi(1 - S_h)^n}{V_{p2}} \quad (\text{A.4})$$

where W is the weighting factor, V_{p1} is the compressional wave velocity computed from the Wood's equation, V_{p2} is the compressional wave velocity calculated from the time-average equation, φ is the porosity of the hydrate-bearing sediments, S_h is the hydrate saturation, and n is a constant which describes the rate of lithification with rising hydrate concentration. As both the time-average equation and Wood's equation fail to apply predictions to the shear wave velocity, in the weighted equation, the shear wave velocity is computed by relating it to the compressional wave velocity through an empirical relation (Lee et al., 1996; Lee and Collett, 2001):

$$V_s = V_p \left[\frac{fV_s}{V_p} \Big|_{\text{solid}} + \frac{fV_s}{V_p} \Big|_{\text{hydrate}} + \frac{fV_s}{V_p} \Big|_{\text{fluids}} \right] \quad (\text{A.5})$$

where the volume fraction of the fluid phase involves water and gas. The weighted equation is established based on the fact that the time-average equation overestimates the wave velocity, normally forming an upper bound, and the Wood's equation underestimates it, providing a lower bound. Therefore the computed results can be adjusted between these two models through tuning the weighting factor and the exponential n . However, when involving the gas phase, both models will underestimate the effective compressional wave velocity. Consequently, a negative weighting factor is required.

Appendix A.4. Biot-Gassmann theory (BGT)

The Biot-Gassmann theory (BGT) has been widely used to provide more physical insights into the elastic properties of hydrate-bearing sediments. The BGT model is expressed as

$$K_{\text{eff}} = K_{ma}(1 - \beta) + \beta^2 M \quad \text{and} \quad G_{\text{eff}} = G_{ma}(1 - \beta) \quad (\text{A.6})$$

where K_{eff} and G_{eff} are effective bulk and shear modulus of the mixture, and K_{ma} and G_{ma} denote the bulk and shear modulus of the matrix. β is the Biot coefficient, which follows the relation: $\beta = 1 - (1 - \varphi)^{3.8}$ for porosity ranges $0 \sim 37\%$ (Lee, 2002a; Krief, 1990). M is calculated by

$$\frac{1}{M} = \frac{\beta - \varphi}{K_{ma}} + \frac{\varphi}{K_{fl}} \quad (\text{A.7})$$

where K_{fl} denotes the bulk modulus of the fluid phase. Typically, by treating the hydrate as different phases (as part of fluid phase or solid matrix), the BGT model can generate two different results. If the hydrate is identified as part of the solid matrix, it occupies the pore space and acts to reduce the porosity, which is also referred to as load-bearing assumption. Otherwise, it only affects the fluid properties and has no effect on the porosity, which is the pore-filling assumption. After introducing the hydrate as either part of the fluid phase or matrix, the bulk and shear modulus of the fluid and the matrix are computed by

$$K = \frac{1}{2} \left[\sum f_i K_i + \left(\sum \frac{f_i}{K_i} \right)^{-1} \right] \quad \text{and} \quad G = \frac{1}{2} \left[\sum f_i G_i + \left(\sum \frac{f_i}{G_i} \right)^{-1} \right] \quad (\text{A.8})$$

where the volume fraction factor term f_i is defined as the volume fraction of i th phase within the matrix or fluid, which is different from the volume fraction of one phase to the bulk. The BGT model enables the calculation of the effective bulk and shear modulus, and the compressional and shear wave velocity can thus be calculated from elastic moduli through equation (3).

References

- Andr , H., Combaret, N., Dvorkin, J., Glatt, E., Han, J., Kabel, M., Keehm, Y., Krzikalla, F., Lee, M., Madonna, C., Marsh, M., Mukerji, T., Saenger, E.H., Sain, R., Saxena, N., Ricker, S., Wiegmann, A., Zhan, X., 2013a. Digital rock physics benchmarks—part II: computing effective properties. *Comput. Geosci.* 50, 33–43. <https://doi.org/10.1016/j.cageo.2012.09.008>.
- Andr , H., Combaret, N., Dvorkin, J., Glatt, E., Han, J., Kabel, M., Keehm, Y., Krzikalla, F., Lee, M., Madonna, C., Marsh, M., Mukerji, T., Saenger, E.H., Sain, R., Saxena, N., Ricker, S., Wiegmann, A., Zhan, X., 2013b. Digital rock physics benchmarks—Part I: imaging and segmentation. *Comput. Geosci.* 50, 25–32. <https://doi.org/10.1016/j.cageo.2012.09.005>.
- Arns, C.H., Knackstedt, M.A., Pinczewski, W.V., Garboczi, E.J., 2002. Computation of linear elastic properties from microtomographic images: methodology and agreement between theory and experiment. *Geophysics* 67, 1396–1405. <https://doi.org/10.1190/1.1512785>.
- Bagherzadeh, S.A., Moudrakovski, I.L., Ripmeester, J.A., Englezos, P., 2011. Magnetic resonance imaging of gas hydrate formation in a bed of silica sand particles. *Energy Fuel.* 25, 3083–3092. <https://doi.org/10.1021/ef200399a>.
- Berge, L.I., Jacobsen, K.A., Solstad, A., 1999. Measured acoustic wave velocities of R11 (CCl₃F) hydrate samples with and without sand as a function of hydrate concentration. *J. Geophys. Res. Solid Earth* 104, 15415–15424. <https://doi.org/10.1029/1999JB900098>.
- Bian, H., Qin, X., Luo, W., Ma, C., Zhu, J., Lu, C., Zhou, Y., 2022. Evolution of hydrate habit and formation properties evolution during hydrate phase transition in fractured-porous medium. *Fuel* 324, 124436. <https://doi.org/10.1016/j.fuel.2022.124436>.
- Borges, J.A., Pires, L.F., C ssaro, F.A., Roque, W.L., Heck, R.J., Rosa, J.A., Wolf, F.G., 2018. X-ray microtomography analysis of representative elementary volume (REV) of soil morphological and geometrical properties. *Soil Tillage Res.* 182, 112–122. <https://doi.org/10.1016/j.still.2018.05.004>.
- Boswell, R., Collett, T.S., 2011. Current perspectives on gas hydrate resources. *Energy Environ. Sci.* 4, 1206–1215. <https://doi.org/10.1039/C0EE00203H>.
- Boswell, R., Yoneda, J., Waite, W.F., 2019. India National Gas Hydrate Program Expedition 02 summary of scientific results: evaluation of natural gas-hydrate-bearing pressure cores. *Mar. Petrol. Geol.* 108, 143–153. <https://doi.org/10.1016/j.marpetgeo.2018.10.020>.

- Buades, A., Coll, B., Morel, J.M., 2011. Non-local means denoising. *Image Process.* Line 1, 208–212. https://doi.org/10.5201/ijp.2011.bcm_nlm.
- Burger, W., Burge, M.J., 2016. Pixel interpolation. In: Burger, W., Burge, M.J. (Eds.), *Digital Image Processing: An Algorithmic Introduction Using Java*. Springer, London. Texts in Computer Science, pp. 539–563. https://doi.org/10.1007/978-1-4471-6684-9_22.
- Chaouachi, M., Falenty, A., Sell, K., Enzmann, F., Kersten, M., 2015. Microstructural evolution of gas hydrates in sedimentary matrices observed with synchrotron X-ray computed tomographic microscopy. *G-cubed* 16, 1711–1722. <https://doi.org/10.1002/2015GC005811>.
- Chen, J., Hu, G., Bu, Q., Liu, C., Dong, L., Wan, Y., Mao, P., Guo, Y., Wang, Z., 2021. Elastic wave velocities of hydrate-bearing sands containing methane gas bubbles: insights from CT-acoustic observation and theoretical analysis. *J. Nat. Gas Sci. Eng.* 88, 103844 <https://doi.org/10.1016/j.jngse.2021.103844>.
- Chen, X., Verma, R., Espinoza, D.N., Prodanović, M., 2018. Pore-scale determination of gas relative permeability in hydrate-bearing sediments using X-ray computed microtomography and lattice Boltzmann method. *Water Resour. Res.* 54, 600–608. <https://doi.org/10.1002/2017WR021851>.
- Costanza-Robinson, M.S., Estabrook, B.D., Fouhey, D.F., 2011. Representative elementary volume estimation for porosity, moisture saturation, and air-water interfacial areas in unsaturated porous media: data quality implications: REV estimation. *Water Resour. Res.* 47 <https://doi.org/10.1029/2010WR009655>.
- Dai, S., Santamarina, J.C., 2014. Sampling disturbance in hydrate-bearing sediment pressure cores: NGHP-01 expedition, Krishna–Godavari Basin example. *Mar. Petrol. Geol.* 58, 178–186. <https://doi.org/10.1016/j.marpetgeo.2014.07.013>.
- Dai, S., Santamarina, J.C., Waite, W.F., Kneafsey, T.J., 2012. Hydrate morphology: physical properties of sands with patchy hydrate saturation: patchy hydrate saturation. *J. Geophys. Res. Solid Earth* 117. <https://doi.org/10.1029/2012JB009667>.
- Darbon, J., Cunha, A., Chan, T.F., Osher, S., Jensen, G.J., 2008. Fast nonlocal filtering applied to electron cryomicroscopy. In: 2008 5th IEEE International Symposium on Biomedical Imaging: from Nano to Macro. IEEE, Paris, France, pp. 1331–1334. <https://doi.org/10.1109/ISBI.2008.4541250>.
- Dong, H., Cui, L., Yu, L., Song, L., Sun, J., Golsanami, N., Liu, X., 2021. New hybrid method for gas-hydrate digital rock reconstruction and its accuracy evaluation. *J. Energy Eng.* 147, 04021050 [https://doi.org/10.1061/\(ASCE\)EY.1943-7897.0000796](https://doi.org/10.1061/(ASCE)EY.1943-7897.0000796).
- Dvorkin, J., Derzhi, N., Diaz, E., Fang, Q., 2011. Relevance of computational rock physics. *Geophysics* 76, E141–E153. <https://doi.org/10.1190/geo2010-0352.1>.
- Dvorkin, J., Nur, A., 1996. Elasticity of high-porosity sandstones: theory for two North Sea data sets. *Geophysics* 61, 1363–1370. <https://doi.org/10.1190/1.1444059>.
- Dvorkin, J., Prasad, M., Sakai, A., Lavoie, D., 1999. Elasticity of marine sediments: rock physics modeling. *Geophys. Res. Lett.* 26, 1781–1784. <https://doi.org/10.1029/1999GL000332>.
- Faisal, T.F., Awedalkarim, A., Chevalier, S., Jouini, M.S., Sassi, M., 2017. Direct scale comparison of numerical linear elastic moduli with acoustic experiments for carbonate rock X-ray CT scanned at multi-resolutions. *J. Petrol. Sci. Eng.* 152, 653–663. <https://doi.org/10.1016/j.petrol.2017.01.025>.
- Garbozzi, E., Day, A., 1995. An algorithm for computing the effective linear elastic properties of heterogeneous materials: three-dimensional results for composites with equal phase Poisson ratios. *J. Mech. Phys. Solid.* 43, 1349–1362. [https://doi.org/10.1016/0022-5096\(95\)00050-5](https://doi.org/10.1016/0022-5096(95)00050-5).
- Goldberg, D., Kleinberg, R., Weinberger, J., 2010. Evaluation of natural gas-hydrate systems using borehole logs. In: *Geophysical Characterization of Gas Hydrates*. Society of Exploration Geophysicists.
- He, G., Luo, X., Zhang, H., Bi, J., 2018. Pore-scale identification of multi-phase spatial distribution of hydrate bearing sediment. *J. Geophys. Eng.* 15, 2310–2317. <https://doi.org/10.1088/1742-2140/aaba10>.
- Helgerud, M.B., Dvorkin, J., Nur, A., Sakai, A., Collett, T., 1999. Elastic-wave velocity in marine sediments with gas hydrates: effective medium modeling. *Geophys. Res. Lett.* 26, 2021–2024. <https://doi.org/10.1029/1999GL000421>.
- Hill, R., 1963. Elastic properties of reinforced solids: some theoretical principles. *J. Mech. Phys. Solid.* 11, 357–372. [https://doi.org/10.1016/0022-5096\(63\)90036-X](https://doi.org/10.1016/0022-5096(63)90036-X).
- Holland, M., Schultheiss, P., Roberts, J., 2019. Gas hydrate saturation and morphology from analysis of pressure cores acquired in the Bay of Bengal during expedition NGHP-02, offshore India. *Mar. Petrol. Geol.* 108, 407–423. <https://doi.org/10.1016/j.marpetgeo.2018.07.018>.
- Hu, G.W., Ye, Y.G., Zhang, J., Liu, C.L., Diao, S.B., Wang, J.S., 2010. Acoustic properties of gas hydrate-bearing consolidated sediments and experimental testing of elastic velocity models. *J. Geophys. Res.* 115, B02102 <https://doi.org/10.1029/2008JB006160>.
- Huaimin, D., Jianmeng, S., Likai, C., Liyuan, S., Weichao, Y., Yafen, L., Zhenzhou, L., Hui, F., 2018. Study on the effects of natural gas hydrate cementation mode on the physical properties of rocks. *J. Geophys. Eng.* 15, 1399–1406. <https://doi.org/10.1088/1742-2140/aab625>.
- Iassonov, P., Gebrenegus, T., Tuller, M., 2009. Segmentation of X-ray computed tomography images of porous materials: a crucial step for characterization and quantitative analysis of pore structures: X-Ray CT image segmentation. *Water Resour. Res.* 45 <https://doi.org/10.1029/2009WR008087>.
- Jakobsen, M., Hudson, J.A., Minshull, T.A., Singh, S.C., 2000. Elastic properties of hydrate-bearing sediments using effective medium theory. *J. Geophys. Res. Solid Earth* 105, 561–577. <https://doi.org/10.1029/1999JB900190>.
- Jin, S., Nagao, J., Takeya, S., Jin, Y., Hayashi, J., Kamata, Y., Ebinuma, T., Narita, H., 2006. Structural investigation of methane hydrate sediments by microfocus X-ray computed tomography technique under high-pressure conditions. *Jpn. J. Appl. Phys.* 45, L714–L716. <https://doi.org/10.1143/JJAP.45.L714>.
- Jin, Y., Konno, Y., Yoneda, J., Kida, M., Nagao, J., 2016. In situ methane hydrate morphology investigation: natural gas hydrate-bearing sediment recovered from the Eastern Nankai Trough Area. *Energy Fuel.* 30, 5547–5554. <https://doi.org/10.1021/acs.energyfuels.6b00762>.
- Jing, L., Hudson, J.A., 2002. *Numerical Methods in Rock Mechanics*, vol. 19.
- Kerker, P., Jones, K.W., Kleinberg, R., Lindquist, W.B., Tomov, S., Feng, H., Mahajan, D., 2009. Direct observations of three dimensional growth of hydrates hosted in porous media. *Appl. Phys. Lett.* 95, 024102 <https://doi.org/10.1063/1.3120544>.
- Kerker, P.B., Horvat, K., Jones, K.W., Mahajan, D., 2014. Imaging methane hydrates growth dynamics in porous media using synchrotron X-ray computed microtomography. *G-cubed* 15, 4759–4768. <https://doi.org/10.1002/2014GC005373>.
- Kleinberg, R.L., Flaum, C., Griffin, D.D., Brewer, P.G., Malby, G.E., Peltzer, E.T., Yesinowski, J.P., 2003. Deep sea NMR: methane hydrate growth habit in porous media and its relationship to hydraulic permeability, deposit accumulation, and submarine slope stability: deep sea nmr. *J. Geophys. Res. Solid Earth* 108. <https://doi.org/10.1029/2003JB002389>.
- Krief, M., 1990. *A Petrophysical Interpretation Using the Velocities of P and S Waves*, vol. 15. Full-Waveform Sonic).
- Kvenvolden, K.A., 1993. Gas hydrates-geological perspective and global change. *Rev. Geophys.* 31, 173–187. <https://doi.org/10.1029/93RG00268>.
- Lee, J.Y., Yun, T.S., Santamarina, J.C., Ruppel, C., 2007. Observations related to tetrahydrofuran and methane hydrates for laboratory studies of hydrate-bearing sediments: study of hydrate-bearing sediments. *G-cubed* 8. <https://doi.org/10.1029/2006GC001531>.
- Lee, M.W., 2002a. Biot–Gassmann theory for velocities of gas hydrate-bearing sediments. *Geophysics* 67, 1711–1719. <https://doi.org/10.1190/1.1527072>.
- Lee, M.W., 2002b. Modified Biot–Gassmann theory for calculating elastic velocities for unconsolidated and consolidated sediments. *Mar. Geophys. Res.* 23, 403–412. <https://doi.org/10.1023/B:MARL.0000018195.75858.12>.
- Lee, M.W., Collett, T.S., 2001. Elastic properties of gas hydrate-bearing sediments. *Geophysics* 66, 763–771. <https://doi.org/10.1190/1.1444966>.
- Lee, M.W., Hutchinson, D.R., Collett, T.S., Dillon, W.P., 1996. Seismic velocities for hydrate-bearing sediments using weighted equation. *J. Geophys. Res. Solid Earth* 101, 20347–20358. <https://doi.org/10.1029/96JB01886>.
- Lei, L., Seol, Y., Choi, J.H., Kneafsey, T.J., 2019. Pore habit of methane hydrate and its evolution in sediment matrix – laboratory visualization with phase-contrast micro-CT. *Mar. Petrol. Geol.* 104, 451–467. <https://doi.org/10.1016/j.marpetgeo.2019.04.004>.
- Lei, L., Seol, Y., Jarvis, K., 2018. Pore-scale visualization of methane hydrate-bearing sediments with micro-CT. *Geophys. Res. Lett.* 45, 5417–5426. <https://doi.org/10.1029/2018GL078507>.
- Lin, Z., Dong, H., Pan, H., Sun, J., Fang, H., Wang, X., 2019. Study on the equivalence between gas hydrate digital rocks and hydrate rock physical models. *J. Petrol. Sci. Eng.* 181, 106241 <https://doi.org/10.1016/j.petrol.2019.106241>.
- Liu, L., Zhang, Z., Li, C., Ning, F., Liu, C., Wu, N., Cai, J., 2020. Hydrate growth in quartzitic sands and implication of pore fractal characteristics to hydraulic, mechanical, and electrical properties of hydrate-bearing sediments. *J. Nat. Gas Sci. Eng.* 75, 103109 <https://doi.org/10.1016/j.jngse.2019.103109>.
- Liu, X., Yin, X., Luan, X., 2018. Seismic rock physical modelling for gas hydrate-bearing sediments. *Sci. China Earth Sci.* 61, 1261–1278. <https://doi.org/10.1007/s11430-017-9214-2>.
- Madadi, M., Jones, A.C., Arns, C.H., Knackstedt, M.A., 2009. 3D imaging and simulation of elastic properties of porous materials. *Comput. Sci. Eng.* 11, 65–73. <https://doi.org/10.1109/MCSE.2009.110>.
- Malagar, B.R., Lijith, K., Singh, D., 2019. Formation & dissociation of methane gas hydrates in sediments: a critical review. *J. Nat. Gas Sci. Eng.* 65, 168–184. <https://doi.org/10.1016/j.jngse.2019.03.005>.
- Millero, F.J., Chen, C.T., Bradshaw, A., Schleicher, K., 1980. A new high pressure equation of state for seawater. *Deep Sea Research Part A. Oceanographic Research Papers* 27, 255–264. [https://doi.org/10.1016/0198-0149\(80\)90016-3](https://doi.org/10.1016/0198-0149(80)90016-3).
- Moridis, G.J., Collett, T.S., Pooladi-Darvish, M., Hancock, S., Santamarina, C., Boswell, R., Kneafsey, T., Rutqvist, J., Kowalsky, M.B., Reagan, M.T., Sloan, E.D., Sum, A.K., Koh, C.A., 2011. Challenges, uncertainties, and issues facing gas production from gas-hydrate deposits. *SPE Reservoir Eval. Eng.* 14, 76–112. <https://doi.org/10.2118/131792-PA>.
- Nobes, D.C., Villinger, H., Davis, E.E., Law, L.K., 1986. Estimation of marine sediment bulk physical properties at depth from seafloor geophysical measurements. *J. Geophys. Res.* 91, 14033 <https://doi.org/10.1029/JB091iB14p14033>.
- Oshima, M., Suzuki, K., Yoneda, J., Kato, A., Kida, M., Konno, Y., Muraoka, M., Jin, Y., Nagao, J., Tenma, N., 2019. Lithological properties of natural gas hydrate-bearing sediments in pressure-cores recovered from the Krishna–Godavari Basin. *Mar. Petrol. Geol.* 108, 439–470. <https://doi.org/10.1016/j.marpetgeo.2019.01.015>.
- Priest, J.A., Best, A.I., Clayton, C.R.I., 2005. A laboratory investigation into the seismic velocities of methane gas hydrate-bearing sand: seismic velocity of hydrate-bearing sand. *J. Geophys. Res. Solid Earth* 110. <https://doi.org/10.1029/2004JB003259>.
- Priest, J.A., Rees, E.V.L., Clayton, C.R.I., 2009. Influence of gas hydrate morphology on the seismic velocities of sands: velocity of hydrate-bearing sands. *J. Geophys. Res. Solid Earth* 114. <https://doi.org/10.1029/2009JB006284>.
- Ren, X., Guo, Z., Ning, F., Ma, S., 2020. Permeability of hydrate-bearing sediments. *Earth Sci. Rev.* 202, 103100 <https://doi.org/10.1016/j.earscirev.2020.103100>.
- Rozenbaum, O., du Roscoat, S.R., 2014. Representative elementary volume assessment of three-dimensional X-Ray microtomography images of heterogeneous materials:

- application to limestones. *Phys. Rev.* 89, 053304 <https://doi.org/10.1103/PhysRevE.89.053304>.
- Sahoo, S.K., Madhusudhan, B.N., Marín-Moreno, H., North, L.J., Ahmed, S., Falcon-Suarez, I.H., Minshull, T.A., Best, A.I., 2018a. Laboratory insights into the effect of sediment-hosted methane hydrate morphology on elastic wave velocity from time-lapse 4-D synchrotron X-Ray computed tomography. *G-cubed* 19, 4502–4521. <https://doi.org/10.1029/2018GC007710>.
- Sahoo, S.K., Marín-Moreno, H., North, L.J., Falcon-Suarez, I., Madhusudhan, B.N., Best, A.I., Minshull, T.A., 2018b. Presence and consequences of coexisting methane gas with hydrate under two phase water-hydrate stability conditions. *J. Geophys. Res. Solid Earth* 123, 3377–3390. <https://doi.org/10.1029/2018JB015598>.
- Santamarina, J.C., Dai, S., Jang, J., Terzariol, M., 2012. Pressure core characterization tools for hydrate-bearing sediments. *Sci. Drill.* 14, 44–48. <https://doi.org/10.5194/sd-14-44-2012>.
- Sell, K., Saenger, E.H., Falenty, A., Chaouachi, M., Haberthür, D., Enzmann, F., Kuhs, W. F., Kersten, M., 2016. On the path to the digital rock physics of gas hydrate-bearing sediments –processing of in situ synchrotron-tomography data. *Solid Earth* 7, 1243–1258. <https://doi.org/10.5194/se-7-1243-2016>.
- Spence, G.D., Haacke, R.R., Hyndman, R.D., 2010. Seismic indicators of natural gas hydrate and underlying free gas. In: *Geophysical Characterization of Gas Hydrates. Society of Exploration Geophysicists*.
- Stoll, R.D., 1974. Effects of gas hydrates in sediments. In: Kaplan, I.R. (Ed.), *Natural Gases in Marine Sediments*. Springer US, Boston, MA, pp. 235–248. https://doi.org/10.1007/978-1-4684-2757-8_4.
- Stoll, R.D., Bryan, G.M., 1979. Physical properties of sediments containing gas hydrates. *J. Geophys. Res.* 84, 1629. <https://doi.org/10.1029/JB084iB04p01629>.
- Tohidi, B., Anderson, R., Clennell, M.B., Burgass, R.W., Biderkab, A.B., 2001. Visual observation of gas-hydrate formation and dissociation in synthetic porous media by means of glass micromodels. *Geology* 29, 867. [https://doi.org/10.1130/0091-7613\(2001\)029;0867:VOOGHF;2.0.CO;2](https://doi.org/10.1130/0091-7613(2001)029;0867:VOOGHF;2.0.CO;2).
- Waite, W.F.W., Winters, W., Mason, D., 2004. Methane hydrate formation in partially water-saturated Ottawa sand. *Am. Mineral.* 89, 1202–1207. <https://doi.org/10.2138/am-2004-8-906>.
- Waite, W.F., Santamarina, J.C., Cortes, D.D., Dugan, B., Espinoza, D.N., Germaine, J., Jang, J., Jung, J.W., Kneafsey, T.J., Shin, H., Soga, K., Winters, W.J., Yun, T.S., 2009. Physical properties of hydrate-bearing sediments. *Rev. Geophys.* 47, RG4003. <https://doi.org/10.1029/2008RG000279>.
- Winters, W., Wilcox-Cline, R., Long, P., Dewri, S., Kumar, P., Stern, L., Kerr, L., 2014. Comparison of the physical and geotechnical properties of gas-hydrate-bearing sediments from offshore India and other gas-hydrate-reservoir systems. *Mar. Petrol. Geol.* 58, 139–167. <https://doi.org/10.1016/j.marpetgeo.2014.07.024>.
- Wood, A., 1960. *A Textbook of Sound: Being an Account of the Physics of Vibrations with Special Reference to Recent Theoretical and Technical Developments*. G. Bell.
- Wu, H., Yao, Y., Zhou, Y., Qiu, F., 2019. Analyses of representative elementary volume for coal using X-ray μ -CT and FIB-SEM and its application in permeability prediction model. *Fuel* 254, 115563. <https://doi.org/10.1016/j.fuel.2019.05.146>.
- Wyllie, M.R.J., Gregory, A.R., Gardner, G.H.F., 1958. An experimental investigation of factors affecting elastic wave velocities in porous media. *Geophysics* 23, 459–493. <https://doi.org/10.1190/1.1438493>.
- Xing, L., Zhu, T., Niu, J., Liu, C., Wang, B., 2020. Development and validation of an acoustic-electrical joint testing system for hydrate-bearing porous media. *Adv. Mech. Eng.* 12, 168781402090898 <https://doi.org/10.1177/1687814020908981>.
- Xue, K., Zhao, J., Song, Y., Liu, W., Lam, W., Zhu, Y., Liu, Y., Cheng, C., Liu, D., 2012. Direct observation of THF hydrate formation in porous microstructure using magnetic resonance imaging. *Energies* 5, 898–910. <https://doi.org/10.3390/en5040898>.
- Yang, L., Zhao, J., Liu, W., Li, Y., Yang, M., Song, Y., 2015. Microstructure observations of natural gas hydrate occurrence in porous media using microfocus X-Ray computed tomography. *Energy Fuel* 29, 4835–4841. <https://doi.org/10.1021/acs.energyfuels.5b00881>.
- Yio, M., Wong, H., Buenfeld, N., 2017. Representative elementary volume (REV) of cementitious materials from three-dimensional pore structure analysis. *Cement Concr. Res.* 102, 187–202. <https://doi.org/10.1016/j.cemconres.2017.09.012>.